CHEMISTRY OF MATERIALS
Cite This: Chem. Mater. 2020, 32, 97−104
Article
pubs.acs.org/cm

Toward New 2D Zirconium-Based Metal−Organic Frameworks: Synthesis, Structures, and Electronic Properties

Amandine Cadiau,[†,⊥] Lilia S. Xie,[‡] Nikita Kolobov,[†] Aleksander Shkurenko,[§] Muhammad Qureshi,[⊥] Mohamed R. Tchalala,[§] Sarah S. Park,[‡] Anastasiya Bavykina,[†] Mohamed Eddaoudi,[§] Mircea Dincă,[‡] Christopher H. Hendon,[∥] and Jorge Gascon*[,†]

[†]KAUST Catalysis Center (KCC), Advanced Catalytic Materials and [§]Functional Materials Design, Discovery and Development Research Group, Advanced Membranes and Porous Materials Center, Division of Physical Sciences and Engineering, King Abdullah University of Science and Technology, Thuwal, Jeddah 23955-6900, Saudi Arabia

[‡]Department of Chemistry, Massachusetts Institute of Technology, 77 Massachusetts Avenue, Cambridge, Massachusetts 02139, United States

[∥]Materials Science Institute, Department of Chemistry and Biochemistry, University of Oregon, Eugene, Oregon 97403, United States

Supporting Information

ABSTRACT: Nowadays, zirconium metal−organic frameworks attract more attention because of their robustness and their easier predictability in terms of topology. Herein, we have been able to control synthetic parameters in order to construct two new 2D MOFs with the same **sql** topology. Both materials, **ACM-10** and **ACM-11**, have been characterized by single-crystal X-ray diffraction, thermogravimetric analysis, and UV−vis spectroscopy. Their textural, electrochemical, and conductivity properties are presented along with the opportunities that these new topologically interesting scaffolds offer for the design of new structures.

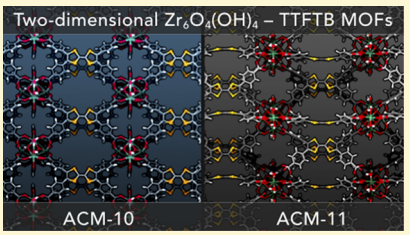

Over the past two decades, metal−organic frameworks (MOFs) have garnered attention because of their structural and compositional tunability, resulting in low-density crystalline solids. Their high porosity has positioned them for applications in gas storage,[1−4] separations,[5−7] or catalysis.[8−10] More recently, MOFs have been studied as potential high-surface area electrodes in electrical devices[11,12] (e.g., chemiresistive sensors[13,14] and electrochemical catalysts[15]). The success of MOFs in these applications depends on the electrical conductivity of the framework itself. Indeed, most MOFs are electrical insulators: charge carrier mobility is typically inversely proportional to crystal density, and many frameworks feature insulating metal−oxide ionic interfaces. To improve the conductivity of MOFs, several strategies have been developed; the most successful installs charge carriers through chemical redox of either the metal/node or ligand.[16−20]

However, chemical stability of the framework is another critical property required for electrically conductive MOF applications. Examination of the literature reveals that frameworks featuring confined ceramic nodes (e.g., the UiO-[21,22] and NU-series[23] and other $Zr_6(O)_4(OH)_4$-containing frameworks) boast improved chemical stability over their late transition metal analogues.[21−25] Zr-based frameworks are known, however, to be primarily electrically insulating even with the inclusion of electroactive guests into the pores.[26,27] Inspired by both the pursuit of a chemically stable and redox active scaffold, we aimed to synthesize novel Zr-based frameworks composed of redox active linkers.

Previous studies have shown that tetrathiafulvalene (TTF) may be singly and doubly oxidized to form stable radical and aromatic adducts, respectively.[28,29] The explicit one-electron oxidation results in the formation of a hole, that is, p-type charge carriers. Electrical conduction is then determined by the extent of the hole delocalization throughout the material, a process that is typically governed by inter TTF−TTF π-stacking interactions. With this in mind, TTF-containing ligands (e.g., tetrathiafulvalene tetrabenzoic acid, TTFTB) have been incorporated into MOFs.[17,30−35] The resultant materials were shown to be modest electrical conductors,[36−40] with the highest performing materials featuring closely packed TTF subunits repeating throughout the crystal.

In contrast, there are a series of materials featuring isolated redox active linkers (rather than π-stacked chains) that still exhibit ligand oxidation.[33,38] In these cases, the oxidation-generated hole is localized, as evidenced by electronic structure calculations and electrical conductivity measurements. Although not conductive, these materials are still interesting as they offer unique routes to store holes in relatively high concentrations (i.e., up to one per ligand), thereby enabling these frameworks to be potentially interesting catalysts.[41−43]

Received: June 24, 2019
Revised: December 17, 2019
Published: December 18, 2019

DOI: 10.1021/acs.chemmater.9b02462
Chem. Mater. 2020, 32, 97−104

Table 1. Selected Crystal Data and Details on Structure Determinations from SCXRD Analysis

	ACM-10	ACM-11
empirical formula	$C_{106.14}H_{129.66}N_{11.38}O_{48.38}S_8Zr_6$	$C_{147.78}H_{174.82}N_{15.26}O_{55.26}S_{12}Zr_6$
formula weight	3142.74	3981.04
crystal system	monoclinic	orthorhombic
space group	*P*2/*m*	*Cccm*
unit cell dimensions	a = 11.9579(7) Å, b = 13.1129(8) Å, c = 20.925(1) Å, β = 98.672(2)°	a = 15.1339(8) Å, b = 27.942(2) Å, c = 42.169(2) Å
volume	3243.5(3) Å^3	17 832(2) Å^3
Z, calculated density	1, 1.609 Mg m^{-3}	4, 1.483 Mg m^{-3}
F(000)	1601	8170
temperature (K)	130.0(1)	296(2)
radiation type, λ	Cu Kα, 1.54178 Å	Cu Kα, 1.54178 Å
absorption coefficient	5.79 mm^{-1}	4.81 mm^{-1}
absorption correction	Multiscan	Multiscan
max and min transmission	0.753 and 0.547	0.127 and 0.048
crystal size	0.02 × 0.03 × 0.03 mm	0.03 × 0.04 × 0.04 mm
shape, color	prism, orange	prism, red-brown
Θ range for data collection	3.4−50.5°	2.1−47.2°
limiting indices	$-11 \le h \le 11$, $-13 \le k \le 13$, $-20 \le l \le 20$	$-14 \le h \le 14$, $-26 \le k \le 26$, $-40 \le l \le 40$
reflection collected/unique/observed with $I > 2\sigma(I)$	38 895/3583 (R_{int} = 0.041)/3247	68 422/4128 (R_{int} = 0.105)/2608
completeness to θ_{max} = 50.5°	99.7%	100.0%
refinement method	Full-matrix least-squares on F^2	Full-matrix least-squares on F^2
data/restraints/parameters	3583/166/386	4128/391/364
final R indices [$I > 2\sigma(I)$]	R_1 = 0.049, wR_2 = 0.136	R_1 = 0.073, wR_2 = 0.219
final R indices (all data)	R_1 = 0.053, wR_2 = 0.139	R_1 = 0.105, wR_2 = 0.254
weighting scheme	$[\sigma^2(F_o^2) + (0.079P)^2 + 16.3732P]^{-1}$[a]	$[\sigma^2(F_o^2) + (0.1482P)^2 + 129.9137P]^{-1}$[a]
goodness-of-fit	1.06	1.05
largest diff. peak and hole	1.61 and −0.80 e Å^{-3}	1.05 and −0.71 e Å^{-3}

[a] $P = (F_o^2 + 2F_c^2)/3$.

Considering these motivations, the combination of a Zr-based $Zr_6(O)_4(OH)_4$ node with a redox active ligand is an attractive platform because the resultant scaffold may feature interesting conductive properties and/or ligand-centered redox chemistry, as well as affording opportunities to install catalytic metals onto/into the Zr-node.[44] TTFTB shares a similar topology to its pyrene analogue; one may expect to form a NU-1000 derivative, but privileged with ligand-centered redox activity. However, upon examination of ∼40 Zr-based MOFs built from quasi-planar tetratopic linkers, the resultant topology depends on whether the Zr-clusters are 12-, 8-, or 6- connected (resulting in 4,12-c **ftw**/**shp**, 4,8-c **csq**/**sqc**/**scu**, and 4,6-c **she**, respectively), which itself depends on the synthetic conditions.[45−47]

The assembly of a single-crystal Zr-TTFTB-containing framework is challenging as there is competition between formation of the strong Zr−carboxylate bond and the π-stacking of the ligands, particularly if the ligands are partially oxidized during synthesis. In this work, through control of the synthetic conditions, we report two crystal structures of Zr-TTFTB, **ACM-10**, and **ACM-11**. Both frameworks are 2D connected and are characterized by single-crystal X-ray diffraction (SCXRD), thermogravimetric analysis (TGA) and UV−vis spectroscopy. Their structural, electrochemical, and conductivity properties are presented, as well as opportunities afforded by these new topologically interesting scaffolds.

EXPERIMENTAL SECTION

All chemicals were acquired from commercial sources and used as obtained. H_4TTFTB was ordered from Chemsoon. Reagent grade solvents were used.

Synthesis of ACM-10, $[Zr_6O_4(OH)_4(H_2O)_2(TTFTB)_2\ (HCOO)_4]\cdot 11.4DMF\cdot 3H_2O$. In a pyrex vial, H_4TTFTB (4.6 mg, 0.007 mmol) was dissolved in a mixture of dimethylformamide (DMF)−H_2O (1 mL:0.25 mL) in the presence of formic acid (0.76 mL). Then, 40 μL of a $ZrOCl_2$ solution (0.5 M) in water was added. The solution was sonicated few minutes before being placed in a preheated oven at 115 °C for 3 days. After cooling down, orange polycrystalline powder was recovered by filtration, washed with acetonitrile, and dried in air. Orange diamond-shaped crystals were obtained using 1 mL of formic acid (Figure S1). The yield, based on zirconium, is 39.4%. Elemental analysis: theoretical N = 5.06%, C = 40.53%, H = 3.93%, and S = 8.15% and experimental N = 4.70%, C = 40.83%, H = 3.41%, and S = 9.14%.

Synthesis of ACM-11, $[Zr_6(O)_4(OH)_4(H_2O)_8(TTFTB)_3]\cdot 7.6DMF$. In a pyrex vial, H_4TTFTB (6.8 mg, 0.01 mmol) was dissolved in DEF (1 mL) in the presence of formic acid (0.57 mL). Then, 40 μL of a $ZrOCl_2$ solution (0.5 M) in water was added. The solution was sonicated few minutes before being placed in a preheated oven at 115 °C for 3 days. After cooling down, dark red square crystals were recovered by filtration, washed with acetonitrile, and dried in air (Figure S1). The yield, based on zirconium, is 62.2%. Elemental analysis: theoretical N = 3.11%, C = 43.77%, H = 3.54%, and S = 11.21% and experimental N = 2.89%, C = 43.51%, H = 3.48%, and S = 11.71%

CCDC 1910185 and 1910226 contain the supplementary crystallographic data for this paper. These data can be obtained free of charge from the Cambridge Crystallographic Data Centre via www.ccdc.cam.ac.uk. Selected crystal data and details on structure determinations are listed in Table 1.

Powder X-ray Diffraction. Powder X-ray diffraction (PXRD) measurements were carried out at room temperature on a Bruker D8 ADVANCE X-ray diffractometer with Cu Kα radiation (λ = 0.154 nm) operated at 40 kV and 40 mA in a Bragg−Brentano geometry with a scan speed of 1 s/step and a step size of 0.02°. For the longer

DOI: 10.1021/acs.chemmater.9b02462
Chem. Mater. 2020, 32, 97−104

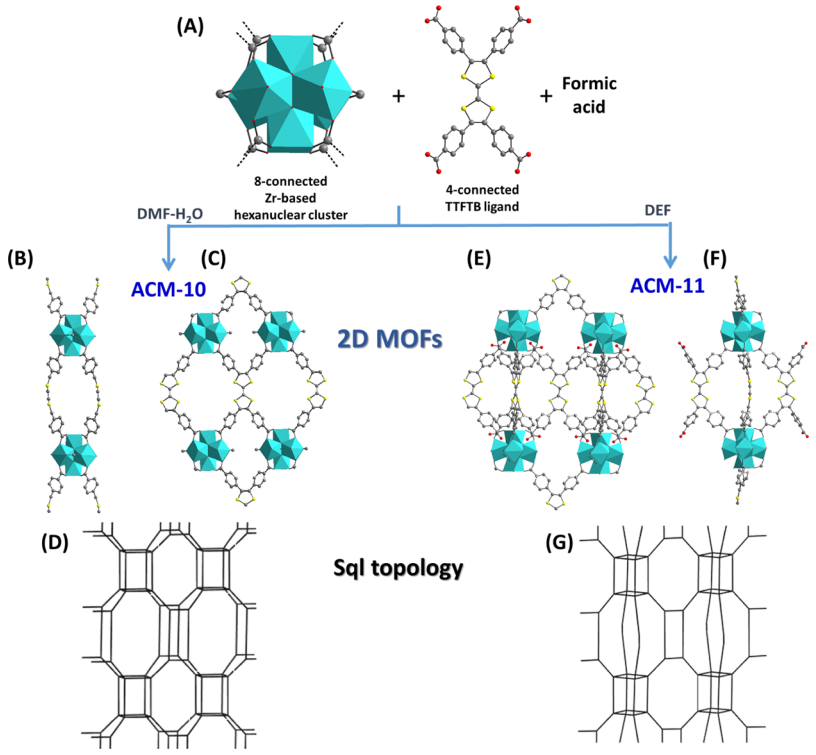

Figure 1. Synthetic path and crystal structures of the two new 2D-ZrMOFs. (A) Building blocks used for the synthesis: the 8-connected inorganic hexanuclear zirconium cluster and 4-connected organic ligand TTFTB building block. (B) One layer of **ACM-10**, view along the *b* axis highlighting the double layer. (C) Crystal structure of **ACM-10**, view along the *a* axis. (D) Representation of the **sql** topology of **ACM-10**. (E) Crystal structure of **ACM-11**, view along the *b* axis. (F) One layer of **ACM-11**, view along the *a* axis highlighting the decorated TTFTB ligand. (G) Representation of the **sql** topology of **ACM-11**.

PXRD measurements necessary for the Le Bail fit, we used a scan speed of 3 s/step and a step size of 0.02°.

Single-Crystal Structure Analysis. Single-crystal X-ray data were collected using a Bruker X8 PROSPECTOR APEX2 CCD diffractometer using Cu Kα radiation (λ = 1.54178 Å). Indexing was performed using APEX2 (difference vectors method).[48] Data integration and reduction were performed using SaintPlus 6.01.[49] Absorption correction was performed by the multiscan method implemented in SADABS.[50] Space groups were determined using XPREP implemented in APEX2.[51] Structures were solved using direct methods (SHELXS-97) and refined using SHELXL-2018/3[52] (full-matrix least-squares on F^2) containing WinGX v1.70.01.[53]

Elemental Analysis. Elemental analysis data were obtained from a ThermoFinnigan apparatus.

Thermogravimetric Analysis. Thermal analyses were conducted on a Mettler Toledo, Thermo Scientific instrument (model TGA/DSC1, Nicolet iS10). Around 3 mg of the sample was subjected to an air flow of 30 mL/min and heated until 900 °C at a rate of 2 °C/min.

Adsorption Analysis. N_2 sorption experiments were performed on a fully automated QUADRASORB SI (Quantachrome Instruments) at relative pressures up to 1 atm. The cryogenic temperatures were controlled using liquid nitrogen bath at 77 K. Samples were exchanged with acetonitrile for 3 days prior experiments and then degassed over night at room temperature under vacuum.

Cyclic Voltammetry. Cyclic voltammetry (CV) of solid-state compounds were performed in a conventional three-electrode electrochemical setup using Pt wire as the counter electrode and Ag/AgCl (sat'd KCl) as the reference electrode. CV was performed at room temperature (298 K) using a 16-channel, research-grade potentiostat system (VMP3; BioLogic Science Instruments). The working electrode was Pt-sputtered onto glass, and then, the dry material was pressed on the surface, followed by few drops of an ethanol/nafion (1:1) mixture and let to dry at room temperature for 15 h.

Conductivity Measurements. Powders were dried under dynamic vacuum for 3 h. Using a home-built two-probe in situ press setup described previously,[37] two-contact probe measurements were carried out at 296 K in an ambient atmosphere on pressed pellets. Linear $I-V$ curves were obtained by sweeping the voltage between −0.5 and +0.5 V and measuring the current using a sourcemeter (Keithley 2450).

Optical Microscope. To determine the morphology of the materials, a Leica DM750 optical microscope equipped with a camera MC170 HD was used.

Diffuse Reflectance UV−Vis Spectroscopy. The optical properties were obtained by using a JASCO V-670 spectrophotometer equipped with an integrating sphere. The diffuse reflectance spectra were recorded in a range of 200−800 nm using halogen and deuterium lamps as light sources. The obtained data were processed using the Kubelka−Munk function.

Calculations. Beginning with the experimentally obtained crystal structure for **ACM-10**, quantum chemical simulations were performed using the DFT framework as implemented in VASP,[54] a commercial software package. The framework was geometrically equilibrated using the PBEsol functional with a Γ-only *k*-grid and a 500 eV planwave cutoff.[55] Convergence criteria were set to <0.005 eV per atom. The electronic band structures were then obtained using the PBEsol geometry computed with the HSE06 functional,[56] sampling five equally spaced low-symmetry k-points along high-symmetry vectors. The electron energies were then aligned to the vacuum level using MacroDensity.[57] **ACM-11** was not computed because of the size of the unit cell and the subtle potential energy surface associated with the H-bonding Zr-bound hydrates.

***ACM-10** Postsynthetic Modification.* **ACM-10** was grafted with Ti(IV) by a method previously reported.[58] All manipulations were performed inside a glovebox under an argon atmosphere. Typically, 30 mg of **ACM-10** was mixed with 2 mL of DMF inside a 10 mL vial. Then, 3.38 μmol $Ti(O^tBu)_4$ was added, and the mixture was transferred to a preheated oven at 100 °C for 24 h. The powder was isolated by centrifugation and washed with DMF, followed by soaking

DOI: 10.1021/acs.chemmater.9b02462
Chem. Mater. 2020, 32, 97−104

in MeOH for 3 days. Finally, the powder was filtered and dried at 160 °C for 4 h.

Photocatalytic Measurements. The photocatalytic hydrogen production experiments were performed in a quartz batch reactor under a continuous Ar flow (2 mL min^{-1}). Samples (**ACM-10** and Ti-grafted **ACM-10**, 20 mg) were suspended in 20 mL of an aqueous solution using 0.1 M L-ascorbic acid as the sacrificial agent with the addition of H_2PtCl_6 as the cocatalyst (3.5 wt % Pt). The suspension was purged with argon prior to photoirradiation by a 300 W Xenon lamp (320−775 nm) or Xenon coupled with the cutoff filter ($\lambda \geq 380$ nm, HOYA L38). The amount of evolved H_2 was measured by gas chromatography (Shimadzu model GC-8A, TCD, Ar gas, molecular sieve 5A).

RESULTS AND DISCUSSION

The use of formic acid as a monotopic modulator resulted in the isolation of two 2D-connected frameworks, **ACM-10** and **ACM-11.** Both crystallize in very similar conditions; in fact our first synthesis led to a mixture of both compounds. However, we later discovered that **ACM-10** can be obtained as a pure phase by adding a small amount of water to the synthesis mixture. Purities of both phases were assessed with Le Bail fits of the PXRD patterns (Figures S2 and S3) and elemental analysis. Single crystals of **ACM-10**, an orange crystalline powder, were obtained using high concentrations of the modulator. Initially, 0.75 mL was used in order to avoid any risk of excess pressurization. Increasing to 1 mL of formic acid yielded orange single crystals. Complementarily, the use of DEF instead of DMF and lower concentration of formic acid led to phase-pure red-brown single crystals of **ACM-11**. Both materials were simplified using the topology rules in a similar way as the convention applied for zeolite. This analysis reveals a **sql** topology (**sql** means the square lattice) where each cluster is connected to four independent ligands. The difference between the two phases, however, arises from the degree of cluster hydration: in **ACM-10**, each linker connects to four different clusters, while in **ACM-11**, half of linkers are connected to four independent clusters and the other half are linked to two independent clusters and have two pendant carboxylates partaking in H-bonding to node-bound water. A similar coordination environment was observed for MgTTFTB.[38]

SCXRD reveals that **ACM-10** crystallizes in a monoclinic system in the space group *P*2/*m*. Each of the six Zr(IV) cations are surrounded by eight oxygen donors, resulting in a hexanuclear cluster (Figure 1A). Four Zr(IV) are bound to two μ_3-OH and two μ_3-O anions, two oxygen atoms from deprotonated carboxylate groups of two independent ligands, one oxygen atom from one deprotonated formate molecule, and one oxygen from either a water molecule or a formate anion. The two other Zr(IV) cations are surrounded by four μ_3-OH/O groups and four oxygen atoms from carboxylate groups of four independent TTFTB. This results in a molecular building block (MBB) formula of $Zr_6(\mu_3\text{-}O)_4(\mu_3\text{-}OH)_4(H_2O)_2(-O_2C)_8$ $(-O_2C)_4$.

One MBB is connected to eight independent TTFTB ligands, and each TTFTB links four independent hexanuclear clusters. The final 2D framework features infinite sheets in the *bc* plane (Figure 1B,C). The topological analysis shows a double **sql** layer constructed from the bridged hexanuclear cluster where carbon atoms of the coordinated carboxylates, acting as points of extension, coincide with the vertices of the square figure of the **sql** net and TTFTB acts as the 4-c node (Figure 1D).

Three types of porous channels can be distinguished in **ACM-10**: two along the *a* axis that exhibit an aperture size of 6.6 and 3 Å, after formate removal, and one along the *b* axis with an aperture of 5.4 Å. The two ligands on both sides, above and below the hexanuclear cluster, present a maximal distance between planes of two TTF cores (>S_2C═CS_2<) of 8.67(1) Å leading to a porous channel along the *b* axis. However, between two layers, $\pi-\pi$ stacking exists with a short plane-to-plane distance of 3.25(1) Å between two ligands. Along the *a* direction, the hexanuclear clusters are linked via strong hydrogen bonding between the water molecules and formate anions with donor-to-acceptor distances of 2.61(1) Å.

ACM-11 crystallizes in the space group *Cccm* with an orthorhombic crystal system. As in **ACM-10**, the inorganic node is built from six Zr(IV) cations to form a hexanuclear cluster (Figure 1A). Two Zr(IV) cations are surrounded by four oxygen atoms from deprotonated carboxylate groups of four independent ligands and by two μ_3-OH and two μ_3-O anions each. Each other four Zr(IV) cations possess two μ_3-O anions, two μ_3-OH, two oxygen atoms from two carboxylate groups belonging to two independent TTFTB, and two oxygens from two water molecules in their coordination sphere.

ACM-11 displays a similar 2D framework with **sql** topology, with infinite sheet connectivity in the *ac* plane (Figure 1G). **ACM-11** can be described as a **sql** layer where the hexanuclear cluster and the TTFTB ligand act as 4-connected nodes (Figure 1E). This layer is further decorated by two ligands in the perpendicular direction, *b* (Figure 1F). These decorative TTFTB ligands exhibit two pendant carboxylates that are hydrogen-bonded to the water molecule of the hexanuclear cluster from the neighbor sheet. **ACM-11** exhibits two kinds of cavities: channels along the axis *a* with an aperture size estimated around 5 Å and cages. Cages have an octahedral shape where two vertexes are the Zr_6 cluster, and the TTF core can be viewed as the other four vertexes. An aperture of 6.2 Å gives access to the cage which exhibits an internal diameter of 9 Å. Here, the shortest distance between two ligands from two neighbor layers is 6.97 Å. The shortest S···S contact distance is 4.89 Å, located between two perpendicular ligands. Both **ACM-10** and **ACM-11** feature multiple node-based sites that could play host to extrinsic metals. The metal-appendage approach has been widely used for other Zr-containing scaffolds,[59] but here, the topology and MBB privilege both structures with the addition of potentially higher metal loadings.

One of our key targets in this work was to synthesize an electronically interesting, stable MOF. We first evaluated the stability of **ACM-10** and **ACM-11**, and the bulk materials were immersed in acetonitrile and water for 24 h. The PXRD pattern of **ACM-10** shows no changes compared to the as-synthesized sample, confirming that its structure is not affected. **ACM-11** was less stable in water as evidenced by the broadening of the peaks (Figures S4 and S5).

The thermal stability of **ACM-10** and **ACM-11** was evaluated using TGA on the as-synthesized samples. Accordingly, the TGA curves exhibit a first weight loss between 100 and 400, and 100 and 300 °C for **ACM-10** and **ACM-11**, respectively, corresponding to solvent departure (Figures S9 and S10). Mass losses are in good agreement with the formula as experimental and theoretical loss values are 28.1 and 27.7, and 18.8 and 20.5%, for **ACM-10** and **ACM-11**, respectively. At temperatures exceeding 400 °C for **ACM-10**

DOI: 10.1021/acs.chemmater.9b02462
Chem. Mater. 2020, 32, 97−104

and 300 °C for **ACM-11**, significant weight reductions are observed and are associated with framework decomposition. The structure analysis combined with TGA supports the presence of permanent microporosity. The nitrogen adsorption−desorption isotherm is presented in Figure S11. The apparent specific Brunauer−Emmett−Teller (BET) surface areas are estimated to be 380 and 420 m^2/g for **ACM-10** and **ACM-11**, respectively. The associated pore volume of **ACM-10** is 0.18 cm^3/g (theoretical PV = 0.17 cm^3/g), while the pore volume of **ACM-11** is 0.25 cm^3/g (theoretical PV = 0.23 cm^3/g).

Electronically, both MOFs have visible absorption features. However, the emergence of color is usually orthogonally related to the conductivity of the framework. UV−vis spectra after Kubelka−Munk transformation are presented in Figure S6. As expected, a significant red shift is observed for **ACM-11** compared to **ACM-10**. Indeed **ACM-10** has a bright orange color, whereas **ACM-11** presents a dark red crystal (Figure S1). Tauc plots (used to extract band gaps) are shown in Figure S6. From this figure, the estimated band gaps are ∼2.16 eV for **ACM-10** and ∼1.9 eV for **ACM-11** (Figures S7 and S8). Most colored MOFs also feature discretized electron energy levels. Explicit ligand redox can typically be probed using electrochemical measurements. CV was performed in acetonitrile with 0.1 M tetrabutylammonium hexafluorophosphate and 2 mg of ferrocyanide and is shown in Figure 2. Using

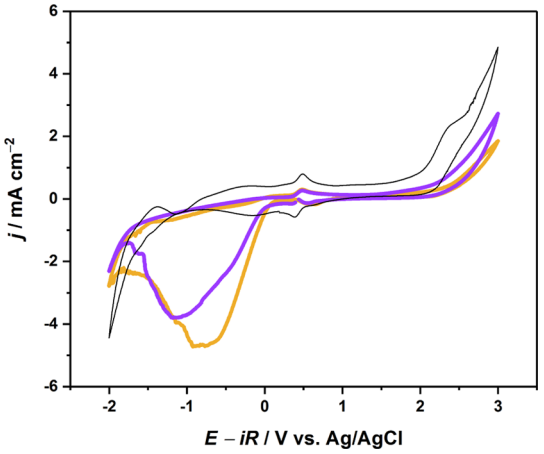

Figure 2. First cyclic voltammogram curve (50 mV s^{-1}) for **ACM-10** (orange) and **ACM-11** (purple) in acetonitrile. Platinum for reference is in black.

a Pt electrode, only the reversible oxidation/reduction of $Fe^{2+/3+}$ at 0.5 V versus Ag/AgCl is observed. The TTF core is known to undergo sequential and reversible oxidations from TTF to the radical cation ($TTF^{+\bullet}$) followed by the dication (TTF^{2+}). However, only one large cathodic current was observed for **ACM-10** and **ACM-11**. Both materials showed a large cathodic current from 0 to −1.5 V versus Ag/AgCl. This peak was irreversible after the first CV, and no corresponding anodic peak was observed (Figure S12). This large cathodic current was ascribed to the reduction of the TTFTB in the MOF.

To investigate the electrical conductivity of **ACM-10** and **ACM-11**, the *I*−*V* curves of two-contact probe-pressed pellet devices were measured for three different batches of each material (Figures S13−S15). **ACM-10** exhibited an average conductivity of $3(2) \times 10^{-10}$ S/cm, with a champion value of $1.3(2) \times 10^{-9}$ S/cm. **ACM-11** exhibited slightly higher conductivities, with an average value of $6(2) \times 10^{-9}$ S/cm and a champion value of $1.8(2) \times 10^{-8}$ S/cm. It is worth mentioning that the conductivities of **ACM-10** and **ACM-11** stayed similar under inert and ambient conditions. The lower conductivity of **ACM-10** and **ACM-11** compared to that of other frameworks based on TTFTB can be attributed to the absence of continuous π-stacking among the TTF moieties in the structure.[35,40] Nevertheless, these conductivity values indicate that intermolecular charge transfer (i.e., hopping) among the ligands is energetically accessible at ambient temperatures, consistent with the crystallographic contact distances.

Although the electrical conductivity is less than desired for sensing and capacitive technologies, quantum chemical simulations reveal unique opportunities for **ACM-10** (see Figure 3). Unlike other Zr-containing frameworks, **ACM-10**

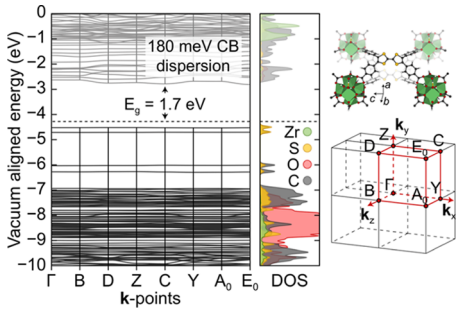

Figure 3. Electronic band structure of **ACM-10**. The electronic band gap matches the red/orange color observed in synthesis. The valence band is composed of highly localized TTFTB-centered orbitals, in line with the diminished TTFTB π-stacking in the crystal. The conduction band features surprisingly disperse bands, attributed to delocalized π electrons in the ligand antibonding orbitals.

features a narrow electronic band gap (computed to be 1.7 eV, in reasonable agreement with experimental data), arising from transitions between relatively high energy TTF-centered and TB-centered orbitals. These high energy electrons are readily liberated (i.e., TTFTB is oxidized), resulting in depletion of the valence band. In principle, these holes would then move through the material, but here, these TTFTB orbitals do not overlap in the crystal (the origin of low conductivity in this case). Meanwhile, the conduction band is relatively dispersed, with comparable electron affinity energetics to the UiO-series,[60] suggesting that similar postsynthetic modification routes may provide access to a chemically stable, visible light-absorbing, catalytic scaffold. For example, one fruitful approach has been the deposition of Ti^{4+} onto the surface of the Zr-nodes. Such approaches did yield catalytic variants of UiO-type materials;[58] their shortcomings have always been the wide electronic band gap and reliance on metals being appended to linker vacant sites. Here, **ACM-10** boasts multiple coordination sites for extrinsic metals, desirable band gap, and ideal chemical stability, making this material compelling for future photocatalytic studies.

Thus, in order to demonstrate the potential application of this framework for photocatalytic applications, we performed the postsynthetic modification of **ACM-10** by Ti(IV) incorporation through the treatment of **ACM-10** with $Ti(O^tBu)_4$ followed by Pt photodeposition (Figure S16). Ti-grafted **ACM-10** with the 0.06/1 Ti/Zr atom ratio exhibits 5.2-

DOI: 10.1021/acs.chemmater.9b02462
Chem. Mater. 2020, 32, 97−104

and 10.8- times improved activity in HER (0.6 and 1.59 μmol h^{-1}) under visible light and UV + vis irradiation, respectively, compare to that of pristine **ACM-10** (Figure 4). Stability was confirmed with PXRD (Figure S17).

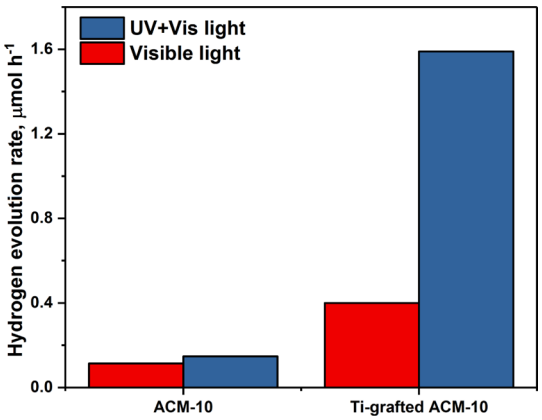

Figure 4. Photocatalytic activity of **ACM-10** and Ti-grafted **ACM-10** in hydrogen production under visible ($\lambda \geq 380$ nm) and UV + vis light (320−775 nm).

CONCLUSIONS

By combining an 8-connected Zr cluster with the tetratopic ligand TTFTB, we synthesized two new Zr-based 2D MOFs. **ACM-10** and **ACM-11** share a **sql** topology that expands in two dimensions and isolates the redox linker at different interplanar distances. The electrical conductivities of **ACM-10** and **ACM-11**, while relatively low, indicate that some charge hopping among the electroactive TTF units is energetically accessible. **ACM-10**, in particular, is predicted to have a large potential for photocatalytic applications, with multiple coordination sites for extrinsic metals, a desirable band gap, and an ideal chemical stability. This hypothesis was experimentally confirmed in photocatalytic hydrogen evolution.

ASSOCIATED CONTENT

Supporting Information

The Supporting Information is available free of charge at https://pubs.acs.org/doi/10.1021/acs.chemmater.9b02462.

Optical images, Le Bail Fit, PXRD, UV−vis, TGA, CV, and I−V curves (PDF)

AUTHOR INFORMATION

Corresponding Author

*E-mail: jorge.gascon@kaust.edu.sa.

ORCID

Aleksander Shkurenko: 0000-0001-7136-2277
Mohamed Eddaoudi: 0000-0003-1916-9837
Mircea Dincă: 0000-0002-1262-1264
Christopher H. Hendon: 0000-0002-7132-768X
Jorge Gascon: 0000-0001-7558-7123

Present Address

[⊥]ICGM, University of Montpellier, CNRS, ENSCM, Montpellier, France

Author Contributions

The manuscript was written through contributions of all authors. All authors have given approval to the final version of the manuscript.

Funding

The work at MIT was supported by the U.S. Department of Energy, Office of Science, Office of Basic Energy Sciences (DE-SC0018235). L.S.X. and S.S.P. thank the National Science Foundation for support through the Graduate Research Fellowship Program (1122374). A.C. thanks the program P.I.A "MOPGA" (APPAT) for funding. This work used the Extreme Science and Engineering Discovery Environment (XSEDE), which is supported by the National Science Foundation grant number ACI-1548562, and the PICS machine, Coeus, which is supported by the NSF (DMS1624776). The KAUST Office of Sponsored Research is gratefully acknowledged for funding through the 2019 CRG program.

Notes

The authors declare no competing financial interest.

REFERENCES

(1) Li, H.; Wang, K.; Sun, Y.; Lollar, C. T.; Li, J.; Zhou, H.-C. Recent advances in gas storage and separation using metal−organic frameworks. *Mater. Today* **2018**, *21*, 108.
(2) Jiang, J.; Furukawa, H.; Zhang, Y.-B.; Yaghi, O. M. High Methane Storage Working Capacity in Metal−Organic Frameworks with Acrylate Links. *J. Am. Chem. Soc.* **2016**, *138*, 10244.
(3) Gygi, D.; Bloch, E. D.; Mason, J. A.; Hudson, M. R.; Gonzalez, M. I.; Siegelman, R. L.; Darwish, T. A.; Queen, W. L.; Brown, C. M.; Long, J. R. Hydrogen Storage in the Expanded Pore Metal−Organic Frameworks M2(dobpdc) (M = Mg, Mn, Fe, Co, Ni, Zn). *Chem. Mater.* **2016**, *28*, 1128.
(4) Bourrelly, S.; Llewellyn, P. L.; Serre, C.; Millange, F.; Loiseau, T.; Férey, G. Different Adsorption Behaviors of Methane and Carbon Dioxide in the Isotypic Nanoporous Metal Terephthalates MIL-53 and MIL-47. *J. Am. Chem. Soc.* **2005**, *127*, 13519.
(5) Cadiau, A.; Adil, K.; Bhatt, P. M.; Belmabkhout, Y.; Eddaoudi, M. A metal-organic framework−based splitter for separating propylene from propane. *Science* **2016**, *353*, 137.
(6) Adil, K.; Belmabkhout, Y.; Pillai, R. S.; Cadiau, A.; Bhatt, P. M.; Assen, A. H.; Maurin, G.; Eddaoudi, M. Gas/vapour separation using ultra-microporous metal−organic frameworks: insights into the structure/separation relationship. *Chem. Soc. Rev.* **2017**, *46*, 3402.
(7) Cadiau, A.; Belmabkhout, Y.; Adil, K.; Bhatt, P. M.; Pillai, R. S.; Shkurenko, A.; Martineau-Corcos, C.; Maurin, G.; Eddaoudi, M. Hydrolytically stable fluorinated metal-organic frameworks for energy-efficient dehydration. *Science* **2017**, *356*, 731.
(8) Rogge, S. M. J.; Bavykina, A.; Hajek, J.; Garcia, H.; Olivos-Suarez, A. I.; Sepúlveda-Escribano, A.; Vimont, A.; Clet, G.; Bazin, P.; Kapteijn, F.; et al. Metal−organic and covalent organic frameworks as single-site catalysts. *Chem. Soc. Rev.* **2017**, *46*, 3134.
(9) Xu, C.; Fang, R.; Luque, R.; Chen, L.; Li, Y. Functional metal−organic frameworks for catalytic applications. *Coord. Chem. Rev.* **2019**, *388*, 268.
(10) Drout, R. J.; Robison, L.; Farha, O. K. Catalytic applications of enzymes encapsulated in metal−organic frameworks. *Coord. Chem. Rev.* **2019**, *381*, 151.
(11) Xu, Y.; Li, Q.; Xue, H.; Pang, H. Metal-organic frameworks for direct electrochemical applications. *Coord. Chem. Rev.* **2018**, *376*, 292.
(12) Stassen, I.; Burtch, N.; Talin, A.; Falcaro, P.; Allendorf, M.; Ameloot, R. An updated roadmap for the integration of metal−organic frameworks with electronic devices and chemical sensors. *Chem. Soc. Rev.* **2017**, *46*, 3185.
(13) Campbell, M. G.; Sheberla, D.; Liu, S. F.; Swager, T. M.; Dincă, M. Cu3(hexaiminotriphenylene)2: An Electrically Conductive 2D

DOI: 10.1021/acs.chemmater.9b02462
Chem. Mater. 2020, 32, 97−104

Metal−Organic Framework for Chemiresistive Sensing. *Angew. Chem., Int. Ed.* **2015**, *54*, 4349.
(14) Campbell, M. G.; Liu, S. F.; Swager, T. M.; Dincă, M. Chemiresistive Sensor Arrays from Conductive 2D Metal−Organic Frameworks. *J. Am. Chem. Soc.* **2015**, *137*, 13780.
(15) Liao, P.-Q.; Shen, J.-Q.; Zhang, J.-P. Metal−organic frameworks for electrocatalysis. *Coord. Chem. Rev.* **2018**, *373*, 22.
(16) D'Alessandro, D. M. Exploiting redox activity in metal−organic frameworks: concepts, trends and perspectives. *Chem. Commun.* **2016**, *52*, 8957.
(17) Su, J.; Yuan, S.; Wang, H.-Y.; Huang, L.; Ge, J.-Y.; Joseph, E.; Qin, J.; Cagin, T.; Zuo, J.-L.; Zhou, H.-C. Redox-switchable breathing behavior in tetrathiafulvalene-based metal−organic frameworks. *Nat. Commun.* **2017**, *8*, 2008.
(18) Li, P.; Wang, B. Recent Development and Application of Conductive MOFs. *Isr. J. Chem.* **2018**, *58*, 1010.
(19) Sun, L.; Campbell, M. G.; Dincă, M. Electrically Conductive Porous Metal−Organic Frameworks. *Angew. Chem., Int. Ed.* **2016**, *55*, 3566.
(20) Ko, M.; Mendecki, L.; Mirica, K. A. Conductive two-dimensional metal−organic frameworks as multifunctional materials. *Chem. Commun.* **2018**, *54*, 7873.
(21) Cavka, J. H.; Jakobsen, S.; Olsbye, U.; Guillou, N.; Lamberti, C.; Bordiga, S.; Lillerud, K. P. A New Zirconium Inorganic Building Brick Forming Metal Organic Frameworks with Exceptional Stability. *J. Am. Chem. Soc.* **2008**, *130*, 13850.
(22) Kandiah, M.; Nilsen, M. H.; Usseglio, S.; Jakobsen, S.; Olsbye, U.; Tilset, M.; Larabi, C.; Quadrelli, E. A.; Bonino, F.; Lillerud, K. P. Synthesis and Stability of Tagged UiO-66 Zr-MOFs. *Chem. Mater.* **2010**, *22*, 6632.
(23) Islamoglu, T.; Otake, K.-i.; Li, P.; Buru, C. T.; Peters, A. W.; Akpinar, I.; Garibay, S. J.; Farha, O. K. Revisiting the structural homogeneity of NU-1000, a Zr-based metal−organic frameworkr. *CrystEngComm* **2018**, *20*, 5913.
(24) Chen, Z.; Hanna, S. L.; Redfern, L. R.; Alezi, D.; Islamoglu, T.; Farha, O. K. Reticular chemistry in the rational synthesis of functional zirconium cluster-based MOFs. *Coord. Chem. Rev.* **2019**, *386*, 32.
(25) Bai, Y.; Dou, Y.; Xie, L.-H.; Rutledge, W.; Li, J.-R.; Zhou, H.-C. Zr-based metal−organic frameworks: design, synthesis, structure, and applications. *Chem. Soc. Rev.* **2016**, *45*, 2327.
(26) Goswami, S.; Ray, D.; Otake, K.-i.; Kung, C.-W.; Garibay, S. J.; Islamoglu, T.; Atilgan, A.; Cui, Y.; Cramer, C. J.; Farha, O. K.; et al. A porous, electrically conductive hexa-zirconium(iv) metal−organic framework. *Chem. Sci.* **2018**, *9*, 4477.
(27) Kung, C.-W.; Otake, K.; Buru, C. T.; Goswami, S.; Cui, Y.; Hupp, J. T.; Spokoyny, A. M.; Farha, O. K. Increased Electrical Conductivity in a Mesoporous Metal−Organic Framework Featuring Metallacarboranes Guests. *J. Am. Chem. Soc.* **2018**, *140*, 3871.
(28) Canevet, D.; Sallé, M.; Zhang, G.; Zhang, D.; Zhu, D. Tetrathiafulvalene (TTF) derivatives: key building-blocks for switchable processes. *Chem. Commun.* **2009**, 2245.
(29) Lorcy, D.; Bellec, N.; Fourmigué, M.; Avarvari, N. Tetrathiafulvalene-based group XV ligands: Synthesis, coordination chemistry and radical cation salts. *Coord. Chem. Rev.* **2009**, *253*, 1398.
(30) Qin, Y.-R.; Zhu, Q.-Y.; Huo, L.-B.; Shi, Z.; Bian, G.-Q.; Dai, J. Tetrathiafulvalene−Tetracarboxylate: An Intriguing Building Block with Versatility in Coordination Structures and Redox Properties. *Inorg. Chem.* **2010**, *49*, 7372.
(31) Wang, H.-Y.; Cui, L.; Xie, J.-Z.; Leong, C. F.; D'Alessandro, D. M.; Zuo, J.-L. Functional coordination polymers based on redox-active tetrathiafulvalene and its derivatives. *Coord. Chem. Rev.* **2017**, *345*, 342.
(32) Wang, H.-Y.; Ge, J.-Y.; Hua, C.; Jiao, C.-Q.; Wu, Y.; Leong, C. F.; D'Alessandro, D. M.; Liu, T.; Zuo, J.-L. Photo- and Electronically Switchable Spin-Crossover Iron(II) Metal−Organic Frameworks Based on a Tetrathiafulvalene Ligand. *Angew. Chem., Int. Ed.* **2017**, *56*, 5465.
(33) Souto, M.; Romero, J.; Calbo, J.; Vitórica-Yrezábal, I. J.; Zafra, J. L.; Casado, J.; Ortí, E.; Walsh, A.; Mínguez Espallargas, G. Breathing-Dependent Redox Activity in a Tetrathiafulvalene-Based Metal−Organic Framework. *J. Am. Chem. Soc.* **2018**, *140*, 10562.
(34) Souto, M.; Santiago-Portillo, A.; Palomino, M.; Vitórica-Yrezábal, I. J.; Vieira, B. J. C.; Waerenborgh, J. C.; Valencia, S.; Navalón, S.; Rey, F.; García, H.; et al. A highly stable and hierarchical tetrathiafulvalene-based metal−organic framework with improved performance as a solid catalyst. *Chem. Sci.* **2018**, *9*, 2413.
(35) Xie, L. S.; Dincă, M. Novel Topology in Semiconducting Tetrathiafulvalene Lanthanide Metal-Organic Frameworks. *Isr. J. Chem.* **2018**, *58*, 1119.
(36) Narayan, T. C.; Miyakai, T.; Seki, S.; Dincă, M. High Charge Mobility in a Tetrathiafulvalene-Based Microporous Metal−Organic Framework. *J. Am. Chem. Soc.* **2012**, *134*, 12932.
(37) Sun, L.; Park, S. S.; Sheberla, D.; Dincă, M. Measuring and Reporting Electrical Conductivity in Metal−Organic Frameworks: Cd2(TTFTB) as a Case Study. *J. Am. Chem. Soc.* **2016**, *138*, 14772.
(38) Park, S. S.; Hendon, C. H.; Fielding, A. J.; Walsh, A.; O'Keeffe, M.; Dincă, M. The Organic Secondary Building Unit: Strong Intermolecular π Interactions Define Topology in MIT-25, a Mesoporous MOF with Proton-Replete Channels. *J. Am. Chem. Soc.* **2017**, *139*, 3619.
(39) Xie, L. S.; Alexandrov, E. V.; Skorupskii, G.; Proserpio, D.; Dincă, M. Diverse $\pi-\pi$ stacking motifs modulate electrical conductivity in tetrathiafulvalene-based metal−organic frameworks. *Chem. Sci.* **2019**, *10*, 8558−8565.
(40) Park, S. S.; Hontz, E. R.; Sun, L.; Hendon, C. H.; Walsh, A.; Van Voorhis, T.; Dincă, M. Cation-Dependent Intrinsic Electrical Conductivity in Isostructural Tetrathiafulvalene-Based Microporous Metal−Organic Frameworks. *J. Am. Chem. Soc.* **2015**, *137*, 1774.
(41) Saouma, C. T.; Tsou, C.-C.; Richard, S.; Ameloot, R.; Vermoortele, F.; Smolders, S.; Bueken, B.; DiPasquale, A. G.; Kaminsky, W.; Valdez, C. N.; et al. Sodium-coupled electron transfer reactivity of metal−organic frameworks containing titanium clusters: the importance of cations in redox chemistry. *Chem. Sci.* **2019**, *10*, 1322.
(42) Saouma, C. T.; Richard, S.; Smolders, S.; Delley, M. F.; Ameloot, R.; Vermoortele, F.; De Vos, D. E.; Mayer, J. M. Bulk-to-Surface Proton-Coupled Electron Transfer Reactivity of the Metal−Organic Framework MIL-125. *J. Am. Chem. Soc.* **2018**, *140*, 16184.
(43) Chambers, M. B.; Wang, X.; Ellezam, L.; Ersen, O.; Fontecave, M.; Sanchez, C.; Rozes, L.; Mellot-Draznieks, C. Maximizing the Photocatalytic Activity of Metal−Organic Frameworks with Aminated-Functionalized Linkers: Substoichiometric Effects in MIL-125-NH2. *J. Am. Chem. Soc.* **2017**, *139*, 8222.
(44) Rimoldi, M.; Howarth, A. J.; DeStefano, M. R.; Lin, L.; Goswami, S.; Li, P.; Hupp, J. T.; Farha, O. K. Catalytic Zirconium/Hafnium-Based Metal−Organic Frameworks. *ACS Catal.* **2017**, *7*, 997.
(45) Wang, H.; Dong, X.; Lin, J.; Teat, S. J.; Jensen, S.; Cure, J.; Alexandrov, E. V.; Xia, Q.; Tan, K.; Wang, Q.; et al. Topologically guided tuning of Zr-MOF pore structures for highly selective separation of C6 alkane isomers. *Nat. Commun.* **2018**, *9*, 1745.
(46) Feng, D.; Gu, Z.-Y.; Chen, Y.-P.; Park, J.; Wei, Z.; Sun, Y.; Bosch, M.; Yuan, S.; Zhou, H.-C. A Highly Stable Porphyrinic Zirconium Metal−Organic Framework with shp-a Topology. *J. Am. Chem. Soc.* **2014**, *136*, 17714.
(47) Lyu, J.; Zhang, X.; Otake, K.-i.; Wang, X.; Li, P.; Li, Z.; Chen, Z.; Zhang, Y.; Wasson, M. C.; Yang, Y.; et al. Topology and porosity control of metal−organic frameworks through linker functionalization. *Chem. Sci.* **2019**, *10*, 1186.
(48) Bruker. *APEX2*, Version 2014.11-0; Bruker AXS Inc.: Madison, Wisconsin, USA, 2014.
(49) Bruker. *SAINT*, Version V8.34A; Bruker AXS Inc.: Madison, Wisconsin, USA, 2014.
(50) Sheldrick, G. M. *SADABS*, Version 2014/5; Bruker AXS Inc.: Madison, Wisconsin, USA, 2008.
(51) Sheldrick, G. M. *XPREP*, Version 2008/2; Brucker AXS Inc.: Madison, Wisconsin, USA, 2008.

DOI: 10.1021/acs.chemmater.9b02462
Chem. Mater. 2020, 32, 97−104

(52) Sheldrick, G. M. Crystal structure refinement with SHELXL. *Acta Crystallogr. C* **2015**, *71*, 3.
(53) Farrugia, L. J. WinGXandORTEP for Windows: an update. *J. Appl. Crystallogr.* **2012**, *45*, 849.
(54) Kresse, G.; Furthmüller, J. Efficiency of ab-initio total energy calculations for metals and semiconductors using a plane-wave basis set. *Comput. Mater. Sci.* **1996**, *6*, 15.
(55) Perdew, J. P.; Ruzsinszky, A.; Csonka, G. I.; Vydrov, O. A.; Scuseria, G. E.; Constantin, L. A.; Zhou, X.; Burke, K. Restoring the Density-Gradient Expansion for Exchange in Solids and Surfaces. *Phys. Rev. Lett.* **2008**, *100*, 136406.
(56) Krukau, A. V.; Vydrov, O. A.; Izmaylov, A. F.; Scuseria, G. E. Influence of the exchange screening parameter on the performance of screened hybrid functionals. *J. Chem. Phys.* **2006**, *125*, 224106.
(57) Butler, K. T.; Hendon, C. H.; Walsh, A. Electronic Chemical Potentials of Porous Metal−Organic Frameworks. *J. Am. Chem. Soc.* **2014**, *136*, 2703.
(58) Santaclara, J. G.; Olivos-Suarez, A. I.; Gonzalez-Nelson, A.; Osadchii, D.; Nasalevich, M. A.; van der Veen, M. A.; Kapteijn, F.; Veber, S. L.; Fedin, M. V.; Murray, A. T.; et al. Revisiting the Incorporation of Ti(IV) in UiO-type Metal−Organic Frameworks: Metal Exchange versus Grafting and Their Implications on Photocatalysis. *Chem. Mater.* **2017**, *29*, 8963.
(59) Yang, D.; Odoh, S. O.; Wang, T. C.; Farha, O. K.; Hupp, J. T.; Cramer, C. J.; Gagliardi, L.; Gates, B. C. Metal−Organic Framework Nodes as Nearly Ideal Supports for Molecular Catalysts: NU-1000- and UiO-66-Supported Iridium Complexes. *J. Am. Chem. Soc.* **2015**, *137*, 7391.
(60) Nasalevich, M. A.; Hendon, C. H.; Santaclara, J. G.; Svane, K.; van der Linden, B.; Veber, S. L.; Fedin, M. V.; Houtepen, A. J.; van der Veen, M. A.; Kapteijn, F.; et al. Electronic origins of photocatalytic activity in d0 metal organic frameworks. *Sci. Rep.* **2016**, *6*, 23676.

DOI: 10.1021/acs.chemmater.9b02462
Chem. Mater. 2020, 32, 97−104